Characterisation and modelling of water wicking and evaporation in capillary porous media for passive and energy-efficient applications

Characterisation and modelling of water wicking and evaporation in capillary porous media for passive and energy-efficient applications – Supplementary Information –

Matteo Alberghini[a,b,c], Svetlana V. Boriskina[a], Pietro Asinari[b,d], Matteo Fasano[b,c,*]

[a] *Massachusetts Institute of Technology, 77 Mass. Ave., Cambridge, MA, USA*
[b] *Politecnico di Torino, Department of Energy, Corso Duca degli Abruzzi 24, Torino, Italy*
[c] *Clean Water Center, Corso Duca degli Abruzzi 24, Torino, Italy*
[d] *Istituto Nazionale di Ricerca Metrologica, Strada delle Cacce 91, Torino, Italy*

---

*Corresponding Author

Supplementary Note 1: Evaluation of the uncertainty

The expanded uncertainty of experimental measurements was estimated as [36]:

$$U = k_u \sqrt{u_A^2 + u_B^2}, \tag{S1}$$

where u_A refers to the component of uncertainty estimated by statistical analysis (type A), u_B refers to the component of uncertainty evaluated by *a priori* information on the instruments used, such as their calibration, accuracy and resolution (type B), and $k_u = 2$ is the coverage factor, in accordance to the NIST standard on uncertainty evaluation [54]. The error bars reported in the figures present an interval of $\pm U$, which, for every measure, is computed as described in the following subsections.

Position of the water front

The standard uncertainty on the *i-th* measurement of the height reached by the water front h_t^i in vertical and horizontal experiments was evaluated as:

$$u_{h_t^i} = \sqrt{\left(\frac{u_s}{2\sqrt{3}}\right)^2 + \left(\frac{u_{f_t^i}}{2\sqrt{6}}\right)^2}, \tag{S2}$$

where $u_s = 2$ mm is the contribution to uncertainty of the depth of dipping (considered as uniformly distributed) and $u_{f_t^i}$ is the thickness of the measured water front at instant t, evaluated from the processed IR images. The contribution to the uncertainty of the caliber resolution was considered negligible. Thus, the uncertainties reported in Figs. 2D and 6D were evaluated as $k_u \cdot u_{h_t^i}$.
The expanded uncertainty on the maximum height reached by the water front h_m was evaluated as:

$$U_{h_m} = k_u \sqrt{\frac{\sum_i^N u_{h_t^i}^2}{N^2} + \frac{R^2}{N}}, \tag{S3}$$

where $R = (\max(h_i) - \min(h_i))/2$ is the evaluation of the A-type component of the uncertainty of the $N = 6$ measurements performed.

Absolute permeability

An equation in the form $h_t = C\sqrt{t}$ was used to fit the experimental data obtained from the horizontal wicking tests (see the inset of Fig. 2D) according to the least squares method. The obtained fitting constant C was used to evaluate the absolute permeability in Eq. 3, thus its expanded uncertainty was evaluated as:

$$U_K = k_u \sqrt{\left(\frac{\partial K}{\partial C} u_C\right)^2 + \left(\frac{\partial K}{\partial \phi}\frac{U_\phi}{k}\right)^2 + \left(\frac{\partial K}{\partial p_c} u_{p_c}\right)^2}, \tag{S4}$$

where $u_C = 5.77 \cdot 10^{-13}$ is the contribution to the uncertainty of the least-squares fitting on the experimental data, $U_\phi = 0.048$ is the expanded uncertainty of the average yarn porosity (see Ref. [4] for further details on the evaluation of U_ϕ) and $u_{p_c} = \rho_w g (U_{h_m}/k)$ is the standard uncertainty of the capillary pressure. Note that the uncertainty on the value of density of the wetting fluid was considered as negligible.

Temperature

The expanded uncertainty of the *i-th* evaluation of temperature shown in Fig. 3B, Figs. 4B-C and Fig. 6B were evaluated as:

$$U_{T,i} = k_u \sqrt{\left(\frac{u_r}{\sqrt{3}}\right)^2 + \left(\frac{u_{TM}}{2}\right)^2 + \left(\frac{u_{FS}}{2}\right)^2}, \tag{S5}$$

where $u_r = 10^{-2}\,^\circ$C is the contribution of the resolution of the digital logger considered as uniformly distributed, $u_{TM} = 10^{-1}\,^\circ$C and $u_{FS} = 0.35\,^\circ$C are respectively the contributions of the sensitivity and the accuracy on the full-scale reading of the thermistors, both considered as normally distributed with a coverage factor $k_u = 2$.
The experimental data reported in Fig. 7B were evaluated by time-averaging the measured temperatures by the thermistors applied on the surface of the heaters, thus their expanded uncertainty was evaluated as:

$$U_T = k_u \sqrt{2\left(\frac{U_{T_i}}{k}\right)^2 + s_{\Delta T}^2}, \tag{S6}$$

where $s_{\Delta T}$ is the standard deviation of the temperature difference between the two thermistors ΔT. The experimental temperature difference shown in Fig. 7C is computed by time-averaging the temperature measurements of the two thermistors placed at the center of the heaters, thus the expanded uncertainty shown was evaluated by Eq. S6.
The uncertainty of the computed temperature trends shown in Fig. 6B (green and black curves) were obtained by averaging the results of 27 simulations. Each simulation was performed using a combination of three parameters, which were varied according to their standard uncertainty: the B-type uncertainty on the measurement of relative humidity, $u_{RH} = 0.025$; the estimated uncertainty on the imbibition time t_i, $u_{t_i} = 0.5$ s; the uncertainty on the convection coefficient h, $u_h = 0.1$ W/(m^{2}K). The 27 simulations considered the possible combinations between the average value of each parameter and the values at the extremes of each interval. The temperature curves reported in Fig. 6B were computed by averaging the simulation results at each considered time-step, while their expanded uncertainties were evaluated by multiplying the standard deviation of the temperatures at each considered time-step for the coverage factor $k_u = 2$.
The computed temperature values reported in Fig. 7B were evaluated by averaging the simulation results obtained by three different values of the air gap thickness,

$[g_a, 2g_a, 3g_a]$, with $g_a = 7.1 \cdot 10^{-5}$ m. Their uncertainty was evaluated as $U_T = k_u \left(\max(T_i) - \min(T_i)\right)/2$, where T_i is the point-dependent temperature value obtained from the *i-th* simulation.

Experimental evaporation rate

The experimental evaporation rate $\bar{m}_{ev}^{exp}$ was evaluated by Eq. S9. Thus, the uncertainty of the *i-th* value was evaluated as:

$$u_{\bar{m}_{ev}^{exp},i} = \left[\left(\frac{\partial \bar{m}_{ev}^{exp}}{\partial \bar{M}_{ev}} u_{\bar{M}_{ev,i}} \right)^2 + \left(\frac{\partial \bar{m}_{ev}^{exp}}{\partial w_i} \frac{u_w}{2\sqrt{3}} \right)^2 + \left(\frac{\partial \bar{m}_{ev}^{exp}}{\partial h_{m,i}} u_{h_{m,i}} \right)^2 \right]^{(1/2)}, \tag{S7}$$

where $u_{\bar{M}_{ev,i}} \sim 10^{-9}$ kg/s is the contribution to uncertainty according to the least-squares fitting method, $u_w = 3 \cdot 10^{-3}$ m is the uncertainty of the measured width of the sample considered as uniformly distributed, and $u_{h_{m,i}}$ is the uncertainty of the *i-th* measurement of the maximum height, evaluated through Eq. S2. The expanded uncertainty $U_{\bar{m}_{ev}^{exp}}$ of the average experimental evaporation rate $\bar{m}_{ev}^{exp}$ was computed as:

$$U_{\bar{m}_{ev}^{exp}} = k_u \sqrt{\frac{\sum_i^N u_{\bar{m}_{ev}^{exp},i}^2}{N^2} + \frac{R^2}{N}}, \tag{S8}$$

where $R = \left(\max(\bar{m}_{ev}^{exp}) - \min(\bar{m}_{ev}^{exp})\right)/2$ is the evaluation of the A-type component of the uncertainty for the $N = 3$ measurements performed.

Supplementary Note 2: Effect of water evaporation on the capillary rise experiments

Since the measured value of h_m might be affected by the evaporation of water, the evaporation rate during the vertical wicking tests was measured to assess its effect on h_m. A high-precision balance (ML204, Mettler Toledo) was used to measure the mass of the textile sample, which increased with time as the water front advanced; h_m was evaluated when the mass of the sample reached the steady state. At this stage, the volume of water evaporating from the sample surface is constantly refilled by the capillary action. As the dipped end of the sample was removed from the water basin, the weight measured by the balance started to decrease linearly with slope $\bar{M}_{ev}$ (measured in kg/s) due to evaporation. Thus, the specific experimental evaporation rate $\bar{m}_{ev}^{exp}$ (measured in kg/(m^{2}s)) could be evaluated as:

$$\bar{m}_{ev}^{exp} = \frac{1}{N} \sum_i^N \frac{\bar{M}_{ev,i}}{2h_{m,i} \cdot w_i}, \tag{S9}$$

where w_i is the width of the *i-th* sample and $N = 3$ is the number of tests averaged. Note that the lateral thickness of the samples, approximately 1% with respect to the frontal surface, was assumed having a negligible effect on the evaporation losses. $\bar{m}_{ev}^{exp}$ was used to model the theoretical effect of evaporation on the wicking performances of the textile.

To assess the relevance of water evaporation from the textile on the measured values of h_m and h_t, the capillary model proposed by the authors in Ref. [4] was used to evaluate the capillary pressure p_c and absolute permeability K for an ideal yarn with the same micro-scale parameters as the textile used (namely, number of fibers per yarn, fibers diameter and yarn porosity). Such capillary model was coupled with the approach proposed by Fries *et al.* [29], which includes the effects of evaporation rate and gravity to Eq. 2 to compute the time-dependent position of the water front h_t. The resulting time-dependent model was implemented with the finite differences approach and used to estimate the possible discrepancy between the height reached by the water front if an evaporation rate of $\bar{m}_{ev}^{exp} = (3.31 \pm 0.11)$ kg/(m^{2}s) (measured through Eq. S9 by averaging the results of three tests performed in laboratory conditions) was considered or neglected. The evaporating and the non-evaporating configurations can be compared considering the instant t when the height of the water front of the configuration considering evaporation is equal to h_m, namely $h_t^{ev} = h_m = 13.8$ cm. At the same instant, the height of the water front of the modelled configuration neglecting evaporation is $h_t^{no-ev} = 14.3$ cm. As this discrepancy is within the uncertainty of the measured value of h_m, water evaporation was neglected in the evaluation of the van Genuchten's parameters L, β and n.

Supplementary Note 3: Modelling of the non homogeneous input heat flux

A schematic of the simulation setup to evaluate the thermal properties of the silicone heaters is reported in Supplementary Fig. S5. The thermal flux provided by the heater Q_{lh} (expressed in W/m^3) was described as a linear function of the radial coordinate with an equal imbalance percentage at the center c_5 and at the border c_6 of the heater, namely:

$$Q_{lh} = (kx + p)/(d_z \pi R^2), \quad \begin{cases} k = P_{in} R^{-1} \left(-c_5 + c_6\right) \\ p = c_5 P_{in} \\ c_5 + c_6 = 0 \end{cases} \tag{S10}$$

where x is the radial coordinate with $x = 0$ at the center of the heater, $R = 5.08$ cm is the radius of the heater and $P_{in} = 1.12$ W is the heat flux experimentally provided to the heater by the power supplier. Convective heat transfer was modelled on the bottom surface of the heater, with

$U_{b,2} = 0.227$ W/(m^{2}K) (evaluated following the procedure described in Supplementary Note 7); whereas, the effect of natural convection on the top surface was evaluated according to Eqs. S14, S15 and S16. The upper part of the heater was considered as a diffuse surface with constant emissivity $\bar{\alpha}_h$. The simulation iteratively adapted the values of c_5 and $\bar{\alpha}_h$ to minimise the difference between the measured temperature of the surface and the numerical results.

Supplementary Note 4: Temperature-dependent physical properties of water and air

The temperature dependent thermophysical properties of water are implemented in the model by means of polynomials in the form:

$$f(T) = AT^3 + BT^2 + CT + D, \tag{S11}$$

where $f(T)$ represents the generic thermophysical property at a specific temperature T, expressed in K. The coefficients of the polynomials are retrieved from the open source software OpenFOAM [55] and are summarised in Tab. S1. Note that, as stated in section 3.1.1, the finite elements implementation of the time-dependent wicking used in this work assumed as constants the density and dynamic viscosity of water. The temperature dependent thermophysical properties of air were evaluated as:

$$\begin{aligned}
\rho_a\,(\mathrm{kg/m^3}) &= \frac{101 \cdot 10^3}{287.058 \cdot T},\\
k_a\,(\mathrm{W/(m \cdot K)}) &= T^5 \cdot 1.5797 \cdot 10^{-17} + T^4 \cdot 9.46 \cdot 10^{-14} + \\
&\quad T^3 \cdot 2.2012 \cdot 10^{-10} - T^2 \cdot 2.3758 \cdot 10^{-7} + \\
&\quad T \cdot 1.7082 \cdot 10^{-4} - 7.488 \cdot 10^{-3},\\
\mu_a\,(\mathrm{Pa \cdot s}) &= T^{1.5} \cdot 1.512 \cdot 10^{-6}(T + 120)^{-1},\\
c_{p,a}\,(\mathrm{J/(kg \cdot K)}) &= T^4 \cdot 1.9327 \cdot 10^{-10} + T^3 \cdot 8 \cdot 10^{-7} + \\
&\quad T^2 \cdot 1.1403 \cdot 10^{-3} - T \cdot 4.489 \cdot 10^{-1} + \\
&\quad 1.0575 \cdot 10^3,
\end{aligned} \tag{S12}$$

with T expressed in K.

Supplementary Note 5: Evaluation of the boundary heat fluxes due to convection and to the insulating box

The polystyrene insulation used in the experimental setup to assess the performance of evaporative cooling (see section 2.3.1) was represented as a 2 cm thick parallelepiped with a 10 cm x 10 cm upper surface. The thermal conductivity of the polystyrene was taken as $k = 0.0325$ W/(m·K). The heat transfer coefficient of the insulating box U_b was evaluated by imposing an inward heat flux (P_{in}, expressed in W) through the circular surface occupied by the textile, supposed isothermal, and measuring the total flux dissipated towards the environment as:

$$U_b = \frac{P_{in}}{A_b\,(T - T_a)}, \tag{S13}$$

where T_a is the ambient temperature, T is the temperature of the isothermal surface providing the inward heat flux, A_b is the total surface of the box exchanging heat with the environment. An adiabatic condition was applied on the lower surface of the domain, which was placed on a plastic support, while the remaining surfaces were assumed to dissipate heat by natural convection. The resulting heat transfer coefficient of the considered setup was evaluated numerically (by finite elements model) as $U_{b,1} = 0.987$ W/(m^{2}K) which was used to estimate the out-of-plane heat flux as $\hat{\mathbf{n}} \cdot \mathbf{q} = q_b = U_{b,1}(T - T_a)$ (see Fig. 6A).
The boundary heat losses due to convection (see Fig. 6A) were evaluated as $\hat{\mathbf{n}} \cdot \mathbf{q} = q_c = h(T - T_a)$, where $T_a = 23.9\,^\circ$C is the average ambient temperature during the tests, and the convection coefficient h for natural convection over an horizontal plate was evaluated as [56]:

$$h = \frac{k_{air}}{\delta_l} \cdot C_h \cdot \mathrm{Ra}^{1/4}, \tag{S14}$$

where δ_l is the characteristic length (ratio between the area and the perimeter of the circular domain), k_{air} is the thermal conductivity of air computed at the average temperature $T_{av} = (T_a + T)/2$, Ra is the Rayleigh number and C_h is a multiplying constant so that [56]:

$$C_h = \begin{cases} 0.54 & \text{if } T_a < T \text{ and } 10^4 \leq \mathrm{Ra} \leq 10^7 \\ 0.27 & \text{if } T_a > T \text{ and } 10^5 \leq \mathrm{Ra} \leq 10^{10}. \end{cases} \tag{S15}$$

The Rayleigh number was evaluated as:

$$\mathrm{Ra} = \frac{g\beta\,(T - T_a)\,L^3 \mathrm{Pr}}{(\mu_a/\rho_a)^2}, \tag{S16}$$

where $\beta \approx 1/T_{av}$ is the approximated expansion coefficient of air [49] and $\mathrm{Pr} = 0.7$ is the Prandtl number of air.

Supplementary Note 6: Effect of the ramp width ω on the imbibition time t_i

The width of the ramp function r used in Eq. 16 was chosen to grant numerical stability to the simulation subsequent to wicking (namely, drying). As a result, the thickness of the obtained water front (see Fig. 5C, namely the distance between the last point with $S_w = 0.99$ and the first point with $S_w = S_0$) is wider than the one appreciable in the IR image in Fig. 2A. Lower values of the ramp width would result in different fitted values of the

	A	B	C	D
Density, ρ_w (kg/m^3)	0	$-3.65471 \cdot 10^{-3}$	1.93017	$7.64025 \cdot 10^{2}$
Thermal conductivity, k_w (W/(m·K))	0	$-9.29827 \cdot 10^{-6}$	$7.1857 \cdot 10^{-3}$	$-7.10696 \cdot 10^{-1}$
Dynamic viscosity, μ_w (Pa·s)	$-2.80572 \cdot 10^{-9}$	$2.90283 \cdot 10^{-6}$	$-1.00523 \cdot 10^{-3}$	$1.16947 \cdot 10^{-1}$
Specific heat, $c_{p,w}$ (J/(kg·K))	$-1.27063 \cdot 10^{-4}$	$1.3736 \cdot 10^{-1}$	$-4.86714 \cdot 10^{1}$	$9.85069 \cdot 10^{3}$

Supplementary Table S1: Coefficients of the polynomials used to model the temperature-dependent properties of water.

van Genuchten's parameters and in a sharper front, but numerical errors arise when the simulation stops to pass from wicking to drying. Since the saturation profile S_w is used in Eq. 25 to compute the wicked volume V_w, it directly affects t_i. To evaluate the effect of ω on t_i, the van Genuchten's parameters were fitted considering $w = 0$ and, consequently, t_i was computed considering the new set of parameters. The resulting values of the van Genuchten's parameters are $L = 0.277$, $\beta = 8.284$ m^{-1} and $n = 5.267$, which produced an imbibition time $t_i = 61.2$ s, only 2.5 s higher than the one estimated with $\omega = 0.8$. This result proves that ω does not affect significantly the outcomes of the simulation, as the wicking transient lasts approximately 60 s while the drying process requires approximately 2000 s.

Supplementary Note 7: Details on the radiative heat transfer model

The incident radiation $I_{rr}(\lambda)$ was studied into two wavelength ranges: the solar radiation in the ultra-violet (UV), visible (VIS) and near-infrared (NIR) range; the thermal emission in the infrared radiation (IR). In the former case, $I_{rr}(\lambda)$ was evaluated from the AM1.5 spectrum; in the latter case, it was evaluated from the temperature-dependent Planck's law:

$$E_r\left(T,\lambda\right) = \frac{2h_P c_l^2}{\lambda^5} \frac{1}{\exp\left(\frac{h_P\, c_l}{k_B \lambda T}\right) - 1}, \tag{S17}$$

where $E_r(T,\lambda)$ is expressed in W/(m^{3}sr), h_P the Planck's constant, c_l the speed of light and k_B the Boltzmann's constant. In the indoor test, the environment is considered as a black-body at the ambient temperature $T = T_a$, while in case of outdoor conditions the environment is considered at $T = T_{sky}$, which was evaluated as a function of the ambient temperature and relative humidity [49]:

$$\begin{aligned} T_{sky} = & T_a \left(0.711 + \left(5.6 \cdot 10^{-2}\right) T_{dp} + \right. \\ & \left. \left(7.3 \cdot 10^{-5}\right) T_{dp}^2\right)^{1/4}, \end{aligned} \tag{S18}$$

where T_a and T_{sky} are expressed in K, T_{dp} is the dew-point temperature expressed in degrees Celsius, which was computed according to the Magnus-Tetens approximation:

$$T_{dp} = c_4 \gamma \left(c_3 - \gamma\right)^{-1}, \tag{S19}$$

where $\gamma = \left(c_3 T_a \left(c_4 + T_a\right)^{-1} + \ln\left(RH\right)\right)$, T_a and T_{dp} are expressed in degrees Celsius, $c_3 = 17.27$ and $c_4 = 237.7$ °C. Note that Eq. S19 is valid in the temperature range $0\,°\text{C} \leq T_a \leq 60\,°\text{C}$.

To reduce the computational cost of simulation, the insulation box was replaced by the boundary heat flux $q_b = U_{b,2}(T - T_a)$ (see Fig. 7A). The insulation properties of the 3-dimensional polystyrene box (8 cm thick, 20 cm x 13 cm upper surface) used to assess the radiative heat transfer properties of the textile were simulated following the same procedure described in section Supplementary Note 5. The thermal conductivity of the polystyrene was set to $k = 0.0325$ W/(m·K); an adiabatic condition was considered on the bottom boundary; natural convection was imposed on the the lateral and the top surfaces; the circular heater was represented as a isothermal and adiabatic surface. Thus, the heat transfer coefficient was evaluated from Eq. S13 by imposing a given heat flux P_{in} (in W) to the circular surface occupied by the heater, and it resulted to be $U_{b,2} = 0.227$ W/(m^{2}K). The heat transfer coefficient h due to natural convection was evaluated through Eqs. S14, S15 and S16, and was used to estimate the convection boundary condition $q_c = h(T - T_a)$ (see Fig. 7A). The lateral heat losses were neglected, thus adiabatic conditions were applied on the right boundaries, while the symmetry condition was imposed on the left boundary.

The four surfaces participating to the radiative heat transfer are the top surface of the heater, the top surface of the fabric and the lateral surfaces of the fabric and the air gap (see Fig. 7A, solid green line). To maintain the adi-

abatic conditions on the lateral surfaces, the lateral sides were supposed to be ideal mirrors facing an environment at their same temperature. Notice that the optical properties of the fabric evaluated experimentally (see section 2.4.1) were concentrated on its top surface, thus the volume enclosed between these four surfaces was considered as transparent. Instead, the heater was supposed to be opaque and its top surface to be optically diffuse. The radiative thermal energy transfer between the fabric and heater can be included in Eq. 21 as boundary heat fluxes $q_{r,i}$, where the subscript i refers to the *i-th* heat source due to radiative heat transfer computed from Eqs. 30, 31, 32 and 33. In particular, when simulating outdoor conditions, the effect of solar radiation was evaluated by Eqs. 30 and 31 with $I_{rr}(\lambda) = \text{AM1.5}$. The optical properties of the fabric in the infrared spectrum were averaged using Eq. 29, where $I_{rr}(\lambda)$ was obtained from Eq. S17 considering $\lambda_i = 2.5\,\mu\text{m}$, $\lambda_e = 20\,\mu\text{m}$ and $T = 50\,^\circ\text{C}$; whereas, the UV-VIS-NIR properties were obtained considering $\lambda_i = 0.25\,\mu\text{m}$, $\lambda_e = 2.5\,\mu\text{m}$ and the AM1.5 spectrum. The average optical properties of the heater in the IR wavelength range were fitted from the temperatures obtained by the uncovered setup. The resulting optical properties employed in the simulation of the fabric and heater are reported in Tab. S2.
The optical properties in the IR range for the wet textile were obtained averaging those of water, considered as black-body in the IR spectrum, and those of the dry textile reported in Tab. S2, that is:

	$\bar{\alpha}$	$\bar{\tau}$	$\bar{r}$
Fabric, IR	0.42	0.25	0.33
Fabric, UV-VIS-NIR	0.17	0.35	0.48
Heater, IR	0.87	0	0.13
Heater, UV-VIS-NIR	0.26	0	0.74

Supplementary Table S2: Optical properties of the dry PE textile and opaque heater from the experimental characterisation.

$$\begin{aligned} \bar{\alpha}_{f,wet} &= S_{nw}\bar{\alpha}_f + S_w, \\ \bar{\tau}_{f,wet} &= S_{nw}\bar{\tau}_f, \\ \bar{r}_{f,wet} &= S_{nw}\bar{r}_f. \end{aligned} \tag{S20}$$

Given the high transparency of water to the solar spectrum and the low thickness of the textile, the optical properties of the wet fabric in the UV-VIS-NIR range were considered as equal to those of the dry textile.
As explained in section 2.4.2, the silicone heater did not supply heat homogeneously to the surface, thus the input heat flux was modelled as a linear function of the radial coordinate. Further details on the simulation procedure used are reported in Supplementary Note 3. Furthermore, the thermistors affected the thermal properties of the heaters surfaces: with a diameter of 2.4 mm, their placement made the surfaces more geometrically irregular than the support of the micro-CT apparatus and, thus, the air gap between the textile and the surface would be on average larger, especially nearby the thermistors. Thus the computations involving the textile were performed considering an homogeneous increased air gap value of $(2g_a \pm g_a)$ (see Fig. 7A). All the simulations described in this section were performed using a stationary solver.

Supplementary Note 8: Effects of the van Genuchten's parameters on the wicking transient

The proposed model was employed to evaluate the effect of the imbibition parameters n, L and β, used in Eqs. 11 and 16, on the capillary water transport. The parameters were swept in the ranges $n = (3 : 3 : 12)$, $L = (0.1 : 0.1 : 0.3)$ and $\beta = (5 : 5 : 20)$, and their effect on the height and thickness of the water front, computed as described in section 3.1.1, was assessed. For the sake of simplicity, the absolute permeability K, evaluated in section 2.2.2, was assumed as constant, justified by considering the permeability of fibrous media as a function of its porosity and fibers arrangement [57].
Supplementary Figs. S6A-B show the saturation profiles after different imbibition times for a small and large value β, namely $\beta = 5$ 1/m and $\beta = 10$ 1/m, varying the parameter n. The results of simulations show that the thickness of the water front, namely how sharp is the transition between $S_w = 1$ and $S_w = 0$, is influenced by the parameter n, while the height of the water front at any given time h_t increases for lower values of β.
Supplementary Figs. S6C-D shows the computed values of h_t and of the water front thickness obtained after 10 minutes of vertical imbibition. To compare the results, both horizontal axes report the ratio between the value used for each parameter (Π) and the respective lower limit in the considered range (Π_0), namely $\Pi_{0,L} = 0.1$, $\Pi_{0,n} = 3$ and $\Pi_{0,\beta} = 5\ \text{m}^{-1}$.
As it can be observed in Supplementary Fig. S6C, the results obtained for the considered ranges of n (blue diamonds) and L (green squares) are scattered, showing that these parameters are not significantly correlated to the height of the water front. On the contrary, h_t is correlated to the parameter β (red circles): lower values β considerably increase the capillary properties, as demonstrated by the exponential fitting curve (solid red line) reported in Supplementary Fig. S6A. Consequently, β also has an affect on the thickness of the water front, as it can be seen by comparing the saturation curves for different values of β (see Supplementary Figs. S6A-B) for the same imbibition time t and value of n. Thus, to estimate the effect of n excluding the bias of β, the latter was used as a blocking factor: the values of the front size obtained for the *i-th* value of β were divided by the minimum value obtained with a given β_i. The results (see Supplementary Fig. S6D) show that the parameter L (green squares) does not affect the normalised front size, while the parameter n (blue diamonds) presents a decreasing exponential correlation with

the investigated property, namely smaller values of n leads to a sharper front.

References

[1] R. Masoodi, K. M. Pillai, Wicking in porous materials: traditional and modern modeling approaches, CRC Press, 2012.

[2] G. Righetti, L. Doretti, H. Sadafi, K. Hooman, S. Mancin, Water pool boiling across low pore density aluminum foams, Heat Transfer Engineering 41 (19-20) (2020) 1673–1682.

[3] M. M. Nahar, B. Ma, K. Guye, Q. H. Chau, J. Padilla, M. Iyengar, D. Agonafer, Microscale evaporative cooling technologies for high heat flux microelectronics devices: Background and recent advances, Applied Thermal Engineering (2021) 117109.

[4] M. Alberghini, S. Hong, L. M. Lozano, V. Korolovych, Y. Huang, F. Signorato, S. H. Zandavi, C. Fucetola, I. Uluturk, M. Y. Tolstorukov, et al., Sustainable polyethylene fabrics with engineered moisture transport for passive cooling, Nature Sustainability 4 (2021) 715–724.

[5] P.-C. Hsu, A. Y. Song, P. B. Catrysse, C. Liu, Y. Peng, J. Xie, S. Fan, Y. Cui, Radiative human body cooling by nanoporous polyethylene textile, Science 353 (6303) (2016) 1019–1023.

[6] B. Dai, K. Li, L. Shi, X. Wan, X. Liu, F. Zhang, L. Jiang, S. Wang, Bioinspired janus textile with conical micropores for human body moisture and thermal management, Advanced Materials 31 (41) (2019) 1904113.

[7] V. Kashyap, H. Ghasemi, Solar heat localization: concept and emerging applications, Journal of Materials Chemistry A 8 (15) (2020) 7035–7065.

[8] M. Morciano, M. Fasano, S. V. Boriskina, E. Chiavazzo, P. Asinari, Solar passive distiller with high productivity and marangoni effect-driven salt rejection, Energy & Environmental Science 13 (10) (2020) 3646–3655.

[9] E. Chiavazzo, M. Morciano, F. Viglino, M. Fasano, P. Asinari, Passive solar high-yield seawater desalination by modular and low-cost distillation, Nature Sustainability 1 (12) (2018) 763–772.

[10] M. Morciano, M. Fasano, L. Bergamasco, A. Albiero, M. L. Curzio, P. Asinari, E. Chiavazzo, Sustainable freshwater production using passive membrane distillation and waste heat recovery from portable generator sets, Applied Energy 258 (2020) 114086.

[11] S. W. Sharshir, M. Elkadeem, A. Meng, Performance enhancement of pyramid solar distiller using nanofluid integrated with v-corrugated absorber and wick: An experimental study, Applied Thermal Engineering 168 (2020) 114848.

[12] X. Li, G. Xu, G. Peng, N. Yang, W. Yu, C. Deng, Efficiency enhancement on the solar steam generation by wick materials with wrapped graphene nanoparticles, Applied Thermal Engineering 161 (2019) 114195.

[13] L. Mascaretti, A. Schirato, R. Zbořil, Š. Kment, P. Schmuki, A. Alabastri, A. Naldoni, Solar steam generation on scalable ultrathin thermoplasmonic tin nanocavity arrays, Nano Energy 83 (2021) 105828.

[14] Y. Chen, Y. Zheng, Bioinspired micro-/nanostructure fibers with a water collecting property, Nanoscale 6 (14) (2014) 7703–7714.

[15] Y. Gao, J. Wang, W. Xia, X. Mou, Z. Cai, Reusable hydrophilic–superhydrophobic patterned weft backed woven fabric for high-efficiency water-harvesting application, ACS Sustainable Chemistry & Engineering 6 (6) (2018) 7216–7220.

[16] M. Rana, J.-T. Chen, S. Yang, P.-C. Ma, Biomimetic superoleophobicity of cotton fabrics for efficient oil–water separation, Advanced Materials Interfaces 3 (16) (2016) 1600128.

[17] M. Alberghini, M. Morciano, M. Fasano, F. Bertiglia, V. Fernicola, P. Asinari, E. Chiavazzo, Multistage and passive cooling process driven by salinity difference, Science advances 6 (11) (2020) eaax5015.

[18] P. Xu, X. Ma, X. Zhao, K. S. Fancey, Experimental investigation on performance of fabrics for indirect evaporative cooling applications, Building and Environment 110 (2016) 104–114.

[19] M. Auliano, D. Auliano, M. Fernandino, P. Asinari, C. A. Dorao, Can wicking control droplet cooling?, Langmuir 35 (20) (2019) 6562–6570.

[20] A. V. Bazilevsky, A. L. Yarin, C. M. Megaridis, Co-electrospinning of core- shell fibers using a single-nozzle technique, Langmuir 23 (5) (2007) 2311–2314.

[21] S. Shen, A. Henry, J. Tong, R. Zheng, G. Chen, Polyethylene nanofibres with very high thermal conductivities, Nature nanotechnology 5 (4) (2010) 251–255.

[22] J. Van Dingenen, High performance dyneema fibres in composites, Materials & Design 10 (2) (1989) 101–104.

[23] C. Balocco, L. Mercatelli, N. Azzali, M. Meucci, G. Grazzini, Experimental transmittance of polyethylene films in the solar and infrared wavelengths, Solar Energy 165 (2018) 199–205.

[24] S. V. Boriskina, An ode to polyethylene, MRS Energy & Sustainability 6 (2019).

[25] Higgs Materials Sustainability Index, `https://msi.higg.org/`, [Online; accessed 10-November-2020].

[26] M. E. Grigore, Methods of recycling, properties and applications of recycled thermoplastic polymers, Recycling 2 (4) (2017) 24.

[27] J. Dees, J. Spruiell, Structure development during melt spinning of linear polyethylene fibers, Journal of Applied Polymer Science 18 (4) (1974) 1053–1078.

[28] G. Vaartstra, L. Zhang, Z. Lu, C. D. Díaz-Marín, J. C. Grossman, E. N. Wang, Capillary-fed, thin film evaporation devices, Journal of Applied Physics 128 (13) (2020) 130901.

[29] N. Fries, K. Odic, M. Conrath, M. Dreyer, The effect of evaporation on the wicking of liquids into a metallic weave, Journal of colloid and interface science 321 (1) (2008) 118–129.

[30] A. Perwuelz, P. Mondon, C. Caze, Experimental study of capillary flow in yarns, Textile Research Journal 70 (4) (2000) 333–339.

[31] Y. Xia, Q. Hou, H. Jubaer, Y. Li, Y. Kang, S. Yuan, H. Liu, M. W. Woo, L. Zhang, L. Gao, et al., Spatially isolating salt crystallisation from water evaporation for continuous solar steam generation and salt harvesting, Energy & Environmental Science 12 (6) (2019) 1840–1847.

[32] N. Xu, X. Hu, W. Xu, X. Li, L. Zhou, S. Zhu, J. Zhu, Mushrooms as efficient solar steam-generation devices, Advanced Materials 29 (28) (2017) 1606762.

[33] Y. Shi, R. Li, Y. Jin, S. Zhuo, L. Shi, J. Chang, S. Hong, K.-C. Ng, P. Wang, A 3d photothermal structure toward improved energy efficiency in solar steam generation, Joule 2 (6) (2018) 1171–1186.

[34] F. Signorato, M. Morciano, L. Bergamasco, M. Fasano, P. Asinari, Exergy analysis of solar desalination systems based on passive multi-effect membrane distillation, Energy Reports 6 (2020) 445–454.

[35] X. Cheng, G. Yang, J. Wu, Recent advances in the optimization of evaporator wicks of vapor chambers: from mechanism to fabrication technologies, Applied Thermal Engineering (2021) 116611.

[36] JCGM, Evaluation of measurement data—guide to the expression of uncertainty in measurement, Int. Organ. Stand. Geneva ISBN 50 (2008) 134.

[37] H. Princen, Capillary phenomena in assemblies of parallel cylinders: I. capillary rise between two cylinders, Journal of Colloid and Interface Science 30 (1) (1969) 69–75.

[38] H. Princen, Capillary phenomena in assemblies of parallel cylinders: Ii. capillary rise in systems with more than two cylinders, Journal of Colloid and Interface Science 30 (3) (1969) 359–371.

[39] M. B. Allen III, Numerical modelling of multiphase flow in porous media, Advances in Water Resources 8 (4) (1985) 162–187.

[40] Y. Mualem, A new model for predicting the hydraulic conductivity of unsaturated porous media, Water resources research 12 (3) (1976) 513–522.

[41] J. Chen, J. Hopmans, M. Grismer, Parameter estimation of two-fluid capillary pressure–saturation and permeability functions, Advances in Water Resources 22 (5) (1999) 479–493.

[42] M. T. Van Genuchten, A closed-form equation for predicting the

hydraulic conductivity of unsaturated soils, Soil science society of America journal 44 (5) (1980) 892–898.
[43] M. Nordlund, V. Michaud, Dynamic saturation curve measurement for resin flow in glass fibre reinforcement, Composites Part A: Applied Science and Manufacturing 43 (3) (2012) 333–343.
[44] COMSOL Multiphysics, Two-phase flow in column, `https://www.comsol.it/model/download/667241/models.ssf.twophase_flow_column.pdf`, [Online; accessed 04-November-2020].
[45] F. E. Jones, Evaporation of water with emphasis on applications and measurements, CRC Press, 1991.
[46] J. Fan, X. Cheng, X. Wen, W. Sun, An improved model of heat and moisture transfer with phase change and mobile condensates in fibrous insulation and comparison with experimental results, International Journal of Heat and Mass Transfer 47 (10-11) (2004) 2343–2352.
[47] A. H. Persad, C. A. Ward, Expressions for the evaporation and condensation coefficients in the hertz-knudsen relation, Chemical reviews 116 (14) (2016) 7727–7767.
[48] G. Somayajulu, New equations for enthalpy of vaporization from the triple point to the critical point, International journal of thermophysics 9 (4) (1988) 567–575.
[49] J. A. Duffie, W. A. Beckman, N. Blair, Solar engineering of thermal processes, photovoltaics and wind, John Wiley & Sons, 2020.
[50] M. Alberghini, M. Morciano, L. Bergamasco, M. Fasano, L. Lavagna, G. Humbert, E. Sani, M. Pavese, E. Chiavazzo, P. Asinari, Coffee-based colloids for direct solar absorption, Scientific reports 9 (1) (2019) 1–11.
[51] H. Li, Pavement materials for heat island mitigation: design and management strategies, Butterworth-Heinemann, 2015.
[52] Y. Zhai, M. Li, S. Gao, L. Yang, H. Zhang, E. Arens, Y. Gao, Indirect calorimetry on the metabolic rate of sitting, standing and walking office activities, Building and Environment 145 (2018) 77–84.
[53] G. Ni, S. H. Zandavi, S. M. Javid, S. V. Boriskina, T. A. Cooper, G. Chen, A salt-rejecting floating solar still for low-cost desalination, Energy & Environmental Science 11 (6) (2018) 1510–1519.
[54] B. N. Taylor, C. E. Kuyatt, Guidelines for evaluating and expressing the uncertainty of nist measurement results (1994).
[55] H. Jasak, A. Jemcov, Z. Tukovic, et al., Openfoam: A c++ library for complex physics simulations, in: International workshop on coupled methods in numerical dynamics, Vol. 1000, IUC Dubrovnik Croatia, 2007, pp. 1–20.
[56] A. Bejan, Convection heat transfer, John wiley & sons, 2013.
[57] M. Karaki, A. Hallal, R. Younes, F. Trochu, P. Lafon, A. Hayek, A. Kobeissy, A. Fayad, A comparative analytical, numerical and experimental analysis of the microscopic permeability of fiber bundles in composite materials, Int. J. Compos. Mater 7 (3) (2017) 82–102.

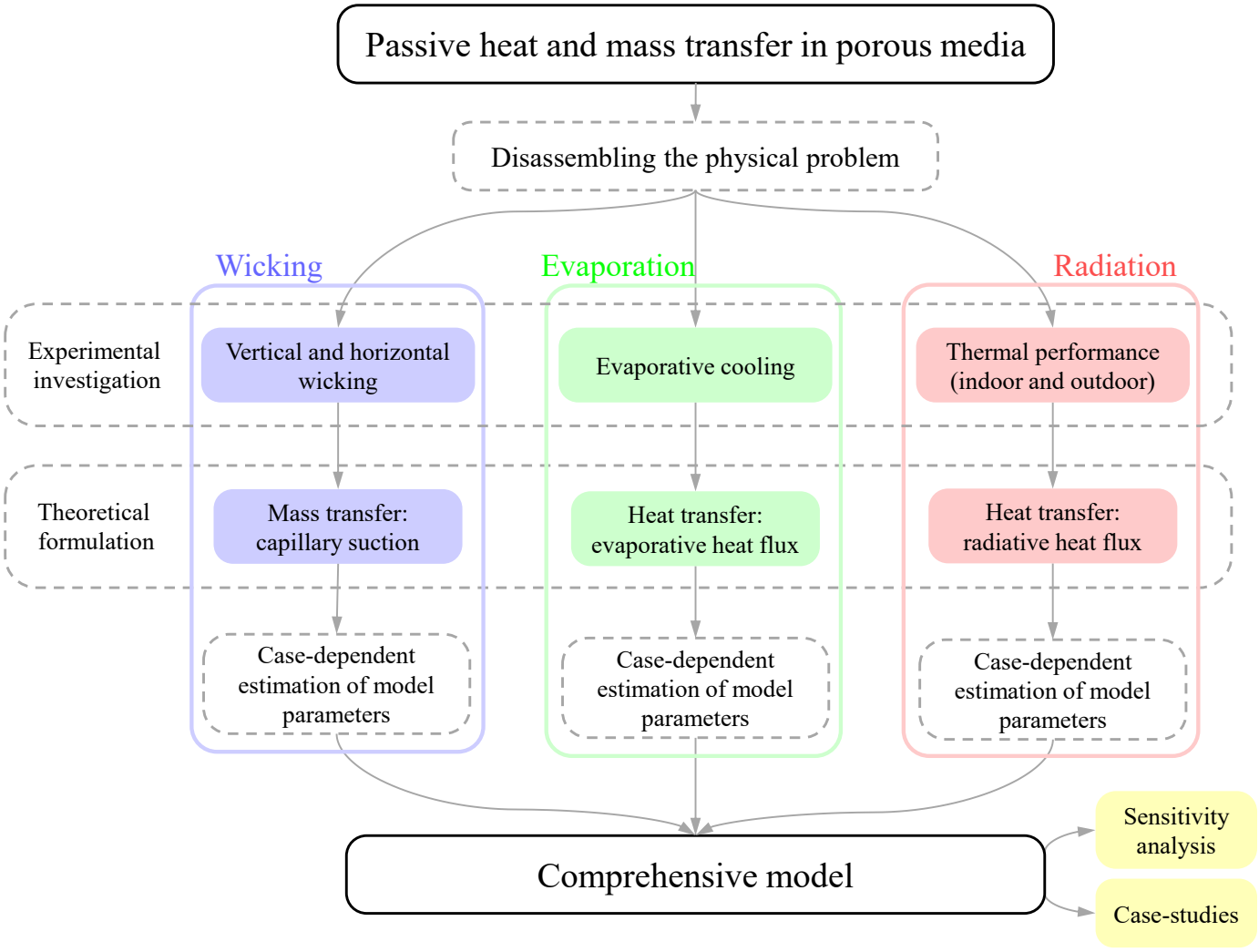

Supplementary Figure S1: **Steps for the characterisation of the passive heat and mass transfer of water in porous media.** The heat and mass transfer process was disassembled into three sub-problem: wicking (blue box), evaporation (green box) and radiation (red box). Each was investigated with a dedicated experimental investigation and theoretical formulation to characterised the proposed porous material. The obtained experimental results were compared with the numerical predictions to estimate the material-dependent parameters of the models. The three sub-models, validated for the tested material, were finally coupled: the comprehensive model could be used to optimise the design of a component by means of sensitivity analyses or application-oriented case-studies. Here, a woven PE textile, specifically designed for personal thermal management, was employed to test and validate the proposed procedure.

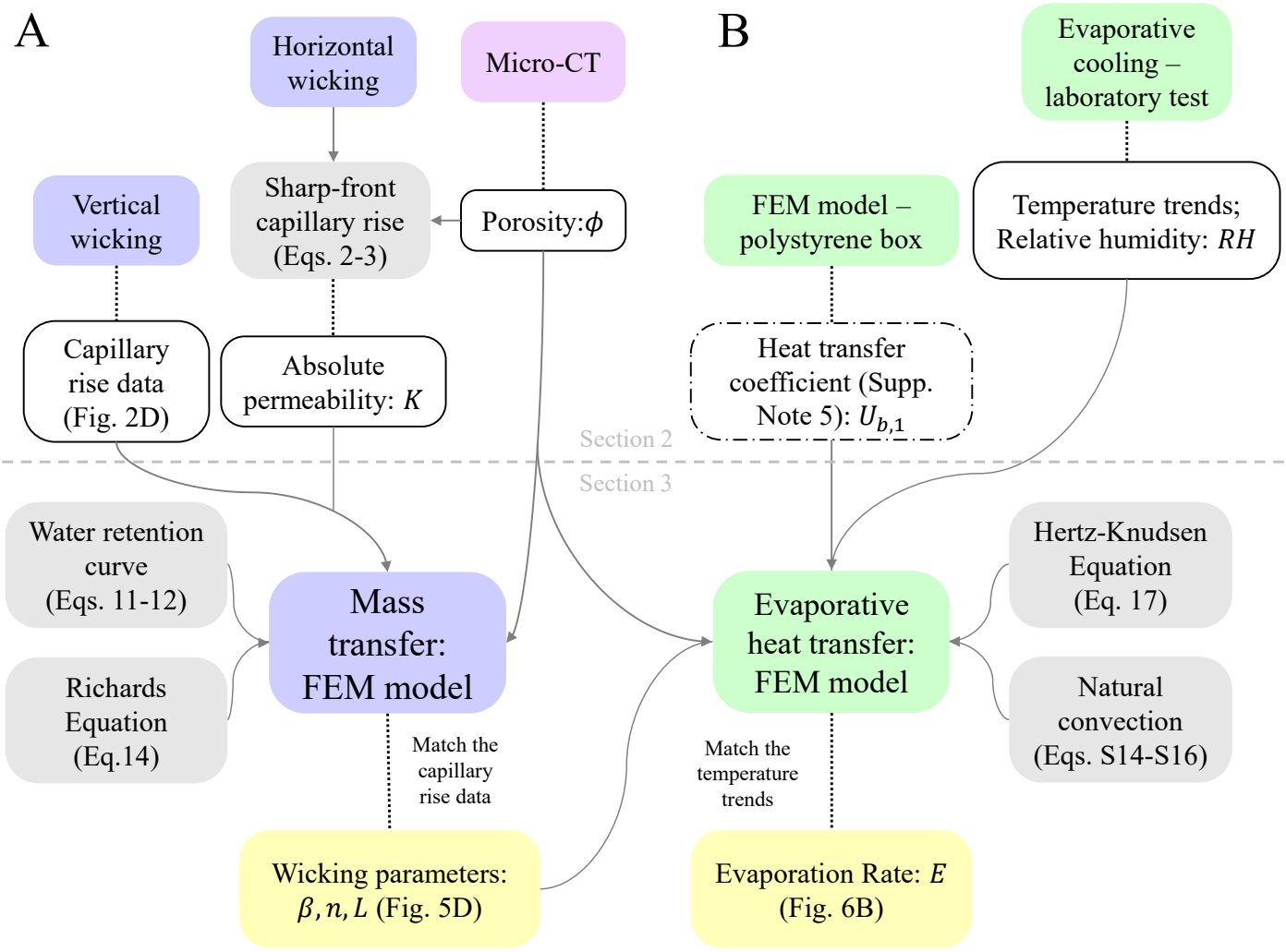

Supplementary Figure S2: **Detailed procedure to investigate wicking and evaporative heat transfer.** Graphical flow-charts of the procedure used to characterise (A) the wicking properties, (B) the evaporation rate in the tested conditions and validate the models. Blue and green boxes report experimental or modelling activity referred to wicking (see sections 2.2.1 and 3.1.1) and evaporative heat transfer (see sections 2.3.1 and 3.2.1), respectively. White boxes indicate the result of each experimental or modelling step; white point-dashed boxes reports the complementary results needed to characterise the experimental setup; the yellow boxes reports the main outcome of the characterisation procedure.

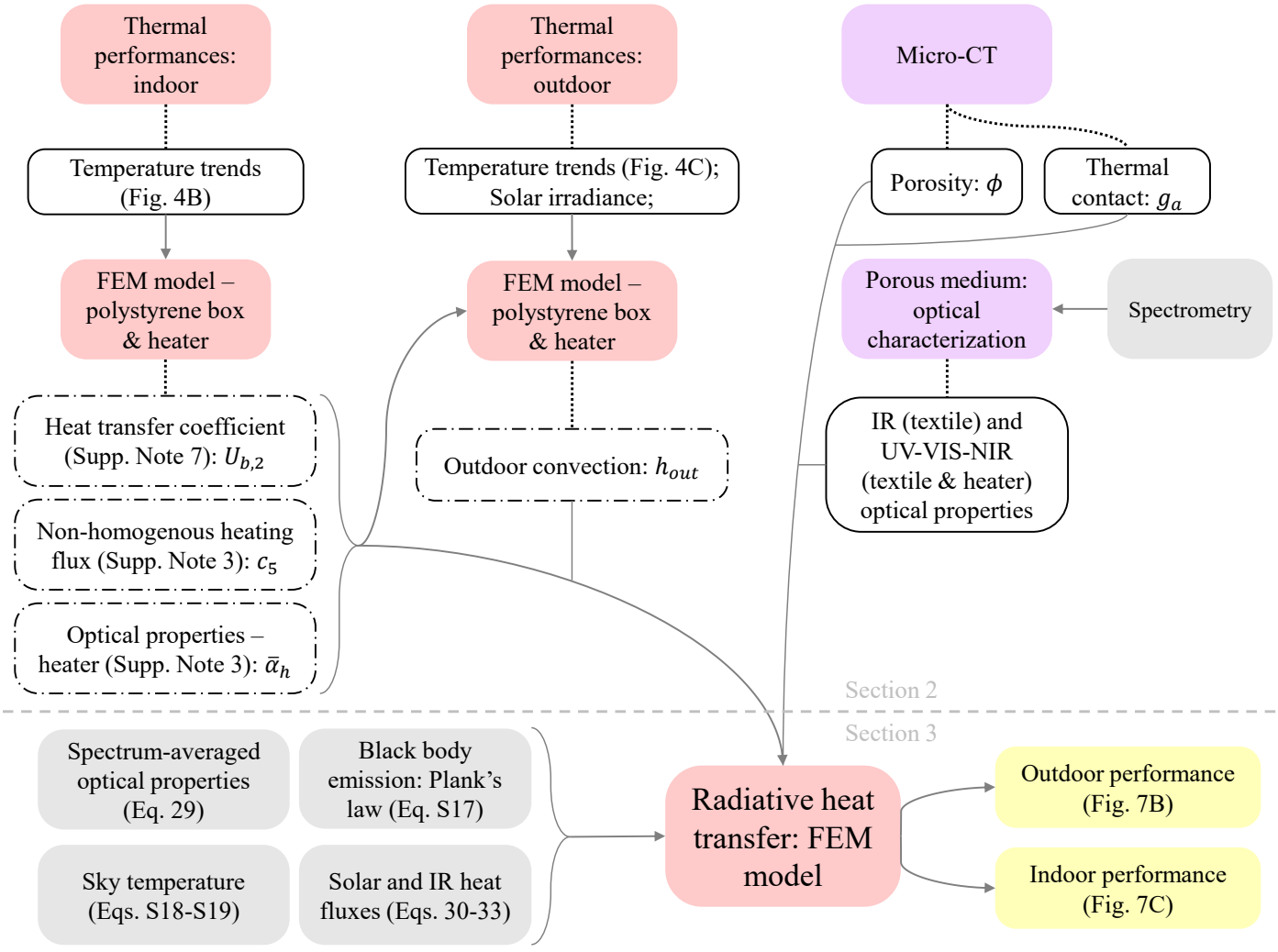

Supplementary Figure S3: **Detailed procedure to investigate radiative heat transfer.** Graphical flow-charts of the procedure to calibrate and validate the radiative heat transfer model. Red boxes refer to experimental or modelling activity described in sections 2.4.1 and 3.3.1, respectively. White boxes indicate the result of each experimental or modelling step; white point-dashed boxes report the complementary results needed to characterise the experimental setup; the yellow boxes report the main outcome of the validation procedure.

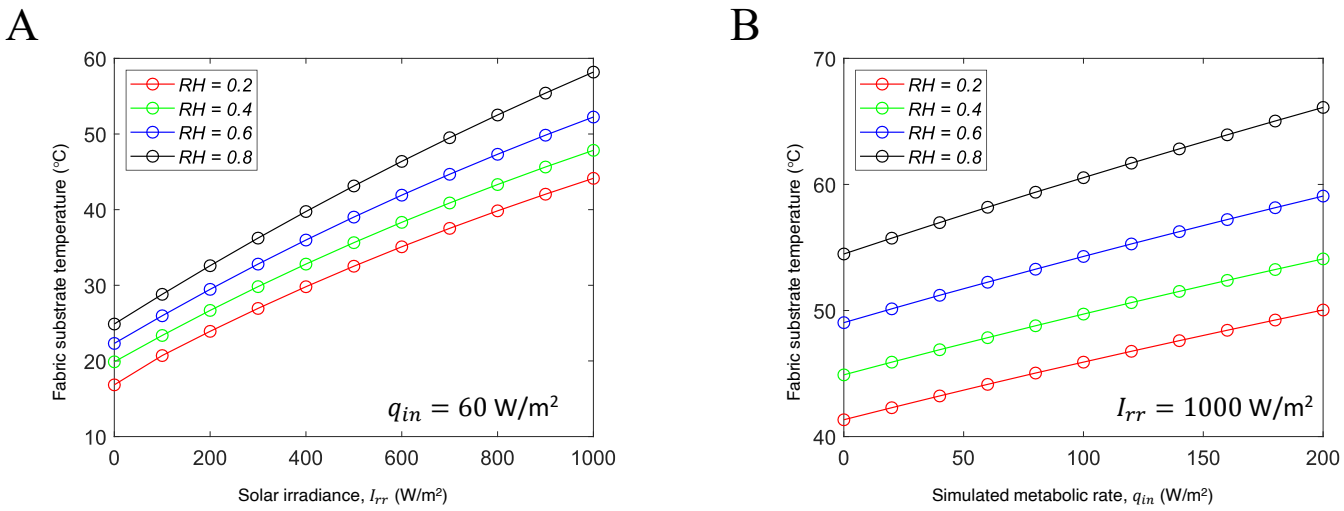

Supplementary Figure S4: **Effect of the environmental conditions on the fabric substrate temperature.** The fabric substrate temperature, namely the temperature of the fabric bottom side in direct contact with the simulated skin, is determined by the fabric thermal and optical properties, the simulated metabolic rate q_{in} and the external conditions T_a, I_{rr}, RH, and can provide an estimation of the user comfort level. (A) Effect of I_{rr} and RH on the fabric substrate temperature at constant $q_{in} = 60$ W/m^2, the usual metabolic rate at rest. The diverging trend of the temperature curves shows the increasing importance of evaporation in hot climates, resulting in a temperature difference of approximately 20 °C at a solar irradiance of 1000 W/m^2. (B) Effect of q_{in} and RH on the fabric substrate temperature at constant $I_{rr} = 1000$ W/m^2, typical of a sunny summer day around noon. The increasing separation between the temperature trends at increasing values of RH show the non-linearity dependence of evaporation with respect to environmental conditions. The analysis reported in panels (A) and (B) were performed considering outdoor conditions at constant ambient temperature $T_a = 25$ °C.

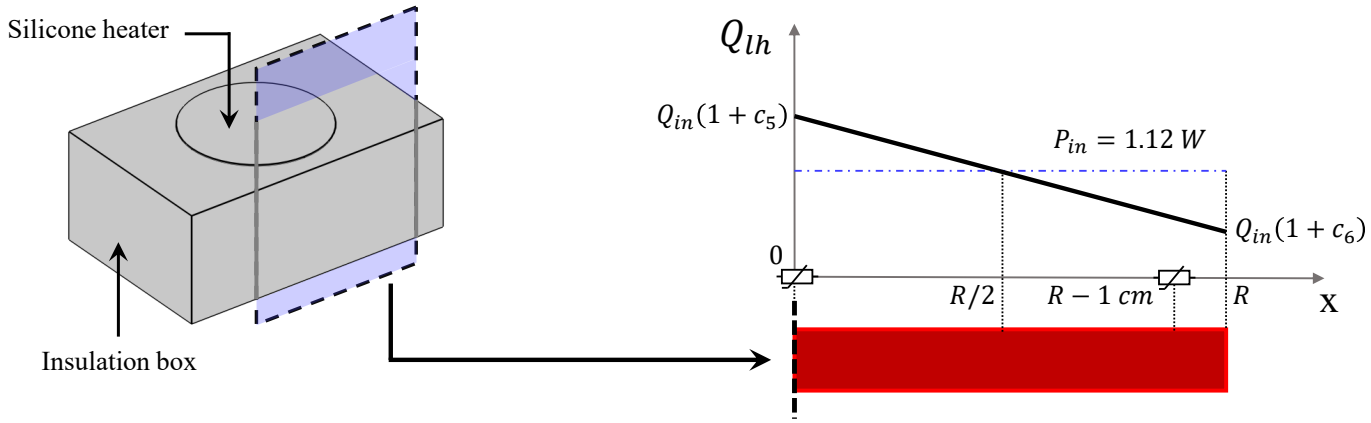

Supplementary Figure S5: Schematics of the 2-dimensional simulation setup used to evaluate the thermal properties of the heaters. To account for the non-homogeneity of the experimental heat flux supplied P_{in}, the simulated input heat flux Q_{lh} was modelled as a linear function P_{in} (dashed blue line), symmetric with respect to $R/2$ and higher at the center of the heater, considering $c_5 = -c_6$, as expressed in Eq. S10. The schematics also reports the positions of the two thermistors placed on the heaters surfaces.

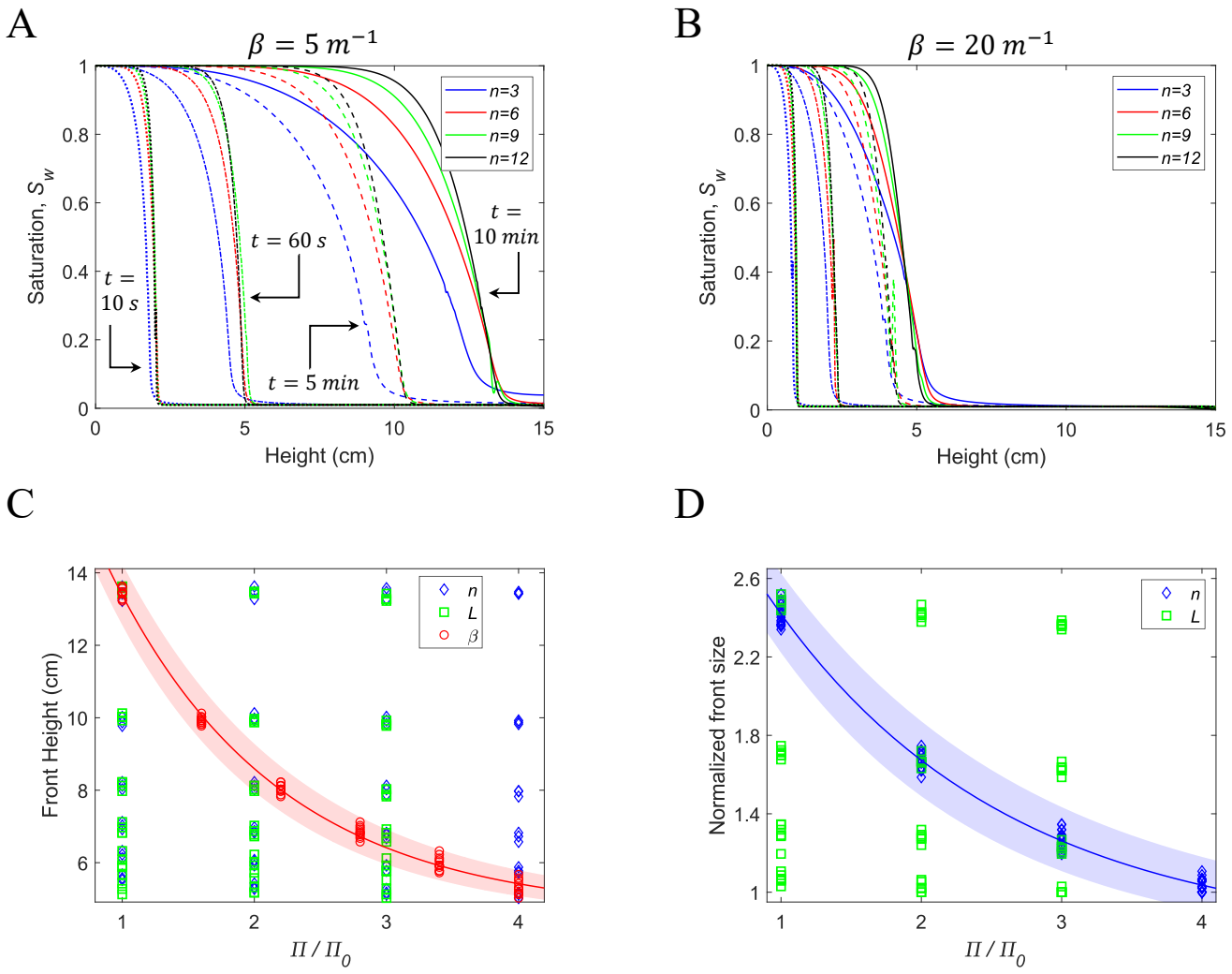

Supplementary Figure S6: **Sensitivity analysis on the wicking parameters.** (A-B) Saturation profiles of the wetting fluid S_w for (A) $\beta = 5$ 1/m and (B) $\beta = 20$ 1/m, varying the parameter n and with $L = 0.3$. The difference between the profiles of S_w is evaluated for $t = 10$ s (dotted curves), $t = 60$ s (dash-dotted curves), $t = 5$ min (dashed curves) and $t = 10$ min (solid curves). (C) Height reached by the water front after 10 minutes of vertical imbibition as a function of the van Genuchten's parameters n (blue diamonds), L (green squares) and β (red circles). To compare the results obtained, the horizontal axis shows, for each parameter, the ratio between the value used for the *i-th* simulation (Π) and the respective lower limit of the tested range (Π_0). The solid red line fits the results with an exponential decay equation and its shaded contour represents the fitting uncertainty with an interval of confidence of 95%. (D) Normalised width of the water front as a function of the van Genuchten's parameter. The normalised plot reveals the dependency between n and the front size. The solid blue line fits the results with an exponential decay equation and its shaded contour represent the fitting uncertainty with an interval of confidence of 95%.